

On Semiparametric Clutter Estimation for Ship Detection in Synthetic Aperture Radar Images

Yi Cui¹, *Member, IEEE*, Jian Yang², *Senior Member, IEEE*, Yoshio Yamaguchi¹, *Fellow, IEEE*, Gulab Singh¹, *Member, IEEE*, Sang-Eun Park¹, *Member, IEEE*, Hirokazu Kobayashi¹, *Senior Member, IEEE*

¹Faculty of Engineering, Niigata University, Niigata, Japan

²Department of Electronic Engineering, Tsinghua University, Beijing, China

The statistical behavior of the sea clutter in synthetic aperture radar (SAR) images is characterized by both the marginal distribution and spatial correlation. However, simultaneous modeling of the joint information remains a difficult job because of the non-Gaussian clutter nature. In this paper, a semiparametric approach is proposed for addressing this problem with the two-fold purpose. First, we investigate the applicability of the nonparametric kernel density estimator (KDE) for marginal distribution estimation of the SAR clutter and show that the KDE is most applicable in the log-intensity domain. Second, we propose to separately estimate the underlying correlation structure with a copula approach and show that the Gaussian copula is a sufficiently accurate model. Consequently, the KDE together with the Gaussian copula, offers a full characterization of the joint probability distribution, based on which a quadratic detector of null distribution is governed by the well-known chi-square law can be conveniently designed for

constant false alarm rate (CFAR) detection. In the experiment, results with both simulated and real SAR data demonstrate that, compared with the single-point detector using only the marginal distribution, the proposed method, which incorporates spatial correlation, significantly improves the detection performance with regard to either the receiver operating characteristic (ROC) curve or detected target pixels. The tradeoff, however, lies in a loss of false alarm rate (FAR) control resulting from increased uncertainty in estimating higher dimensional distributions.

Index Terms—Clutter estimation, copula, kernel density estimator (KDE), ship detection, synthetic aperture radar (SAR).

I. INTRODUCTION

In recently years, ship surveillance has gained a great attention owing to the increasing maritime concerns, for example on piracy and illegal fishing. In particular, ship detection via synthetic aperture radar (SAR) has become a popular choice, due its many advantages including the all-time/all-weather operational capability, high resolution, wide coverage, etc. Especially, with the launch of several state-of-the-art SAR systems, applications have been reported using such as TerraSAR-X [1], RADARSAT-2 [2], and ALOS-PALSAR [3].

Statistical modeling of the sea clutter plays a key role in ship detection because construction of the target detector often requires knowledge of the clutter distribution. In addition, it is also desired that a constant false alarm rate (CFAR) property is ensured so that the clutter must be locally estimated. In the context of ship detection in SAR images, in particular, local estimation of the sea clutter distribution is usually accomplished by a moving reference window which is divided into the test region, the guard

region, and the clutter region as shown in Fig. 1. Suppose the samples within the test region are $\mathbf{X} = (X_1, X_2, \dots, X_d)^T$. Our purpose is then to put \mathbf{X} under hypothesis testing which, as previously mentioned, requires the knowledge of its PDF ($\mathbf{x}|H_0$) where H_0 denotes the null hypothesis. In principle, this PDF can be estimated with the samples drawn from the clutter region of the reference window. For the simplest case when the test region consists of one pixel ($d = 1$), we only have to estimate a univariate marginal PDF $p(x|H_0)$. This is a well studied problem and there exist quite a number of available models [4]–[9]. However, if the test region encompasses multiple pixels (e.g. $d = 9$ for a 3×3 test region), then we have to estimate the joint PDF $p(x_1, x_2, \dots, x_d|H_0)$ which can be a much more difficult task. One reason is that the sea clutter in SAR images exhibits extremely non-Gaussian nature and many empirical models such as the K distribution do not have analytically tractable joint PDF forms. Moreover, from the clutter region we only have one realization of the random process with which directly estimating the higher dimensional (multivariate) PDF becomes less efficient and accurate.

Nevertheless, despite of the difficulty involved in joint distribution estimation, it is expected that the detection performance will be improved because by specifying the joint distribution we have implicitly incorporated the correlation information among neighboring pixels. The purpose of this paper is thus to provide a reliable and tractable way for doing so. We propose to estimate the joint distribution by separately considering its marginal distribution and correlation structure. More specifically, in this paper a semiparametric approach is adopted. We use the nonparametric kernel density estimator (KDE) [10] for estimating the marginal PDF and for characterizing the spatial correlation we introduce a parametric

(Gaussian) copula model [11]. The paper is organized as follows. In Section II, the problem of estimating the marginal PDF of the SAR clutter using KDE is studied and its applicability in different data domains is evaluated. In Section III, the copula approach to incorporate correlation structure is introduced and corresponding target detectors are constructed. In Section IV, experimental results with both simulated and real SAR data are given. Finally, Section V concludes the paper.

II. MARGINAL DISTRIBUTION ESTIMATION USING KERNEL DENSITY ESTIMATOR

In this section, we study the use of the KDE (cf. Appendix for a review) for estimating the marginal distribution of the sea clutter in SAR images. Two previous works are worth mentioning. Jiang et al [12] first used a probabilistic neural network (PNN) for modeling the clutter in the intensity data domain and it was later pointed out that the PNN is equivalent to the KDE [13]. Gao [14] also designed a ship detection algorithm based on the KDE but in the amplitude domain. In both applications, the Gaussian kernel function with a constant and empirically determined bandwidth is used. However, as will be shown in Section II-A, due to the multiplicative noise nature, an adaptive rather than a constant kernel bandwidth is generally needed for the intensity/amplitude data. Instead, in Section II-B we propose to use the KDE in the log-intensity domain and show that a constant kernel bandwidth is admitted therein. Performance comparison in Section II-D also shows that using the KDE in the log-intensity domain enjoys accuracy improvement over its intensity and amplitude counterparts.

A. KDE in the Intensity Domain

For intensity SAR images, it is well-known that the pixel value $I(x, y)$ can be modeled by the following product process [15]:

$$I(x, y) = \sigma(x, y)n(x, y), \quad (1)$$

where $\sigma(x, y)$ is the underlying scattering coefficient, which is spatially but slowly varying; $n(x, y)$ is a stationary random process. In the following, $\sigma(x, y)$ is considered locally constant due to its slow variation so that local stationarity can be assumed for $I(x, y)$. Then whenever unambiguous, we will drop the spatial index for conciseness. If using the KDE to fit the intensity data, the asymptotic optimal bandwidth associated with a Gaussian kernel function is given by (cf. Appendix):

$$h_{\text{opt}} = \left\{ \frac{1}{2\sqrt{\pi}N \int_{-\infty}^{+\infty} [p_n''(x)]^2 dx} \right\}^{\frac{1}{5}} \sigma, \quad (2)$$

where $p_n(x)$ is the marginal PDF of the product noise n and N is the number of samples available for distribution fitting. The above equation shows h_{opt} is linearly proportional to the local scattering coefficient σ . Thus a global bandwidth is generally not suitable for the entire image. One solution is to estimate an initial optimal bandwidth h_{opt}^0 with samples from a selected homogeneous region and to amend it with the local scattering coefficient estimate. Specifically, according to the proportional relationship of Equation (2) the local optimal bandwidth h_{opt} can be written as:

$$h_{\text{opt}} = \left(\frac{N_0}{N} \right)^{\frac{1}{5}} \frac{\hat{\sigma}}{\hat{\sigma}_0} h_{\text{opt}}^0, \quad (3)$$

where $\hat{\sigma}_0$ is the scattering coefficient estimate of the selected homogeneous region and N_0 is the number of samples therein; $\hat{\sigma}$ is the local scattering coefficient estimate and N is the number of samples in the clutter region of the reference window.

It should be noted that the above analysis is also applicable for the amplitude data because the product model given in Equation (1) still holds in the amplitude domain. Hence the procedures of

applying the KDE in both the intensity and amplitude domains are essentially the same but the performances may be subject to change, which will be seen in Section II-D later.

B. KDE in the Log-Intensity Domain

Instead of directly applying the KDE in the intensity domain, we now reconsider its usage with the logarithmically transformed data, *i.e.*, $\ln I$. In this log-intensity domain, the optimal kernel bandwidth is given by (cf. Appendix):

$$h_{\text{opt}} = \left\{ \frac{1}{2\sqrt{\pi}N \int_{-\infty}^{+\infty} \{[p_n(e^x)e^x]^n\}^2 dx} \right\}^{\frac{1}{5}}, \quad (4)$$

where $p_n(x)$ also denotes the marginal PDF of the product noise n . Note that in Equation (4) the optimal kernel bandwidth is independent of the local scattering coefficient so that a global kernel bandwidth is admitted. This fact frees us from locally changing the kernel bandwidth and all we need to do is to rescale the estimated kernel bandwidth from the selected homogenous region with respect to the change of sample numbers, *i.e.*,

$$h_{\text{opt}} = \left(\frac{N_0}{N} \right)^{\frac{1}{5}} h_{\text{opt}}^0, \quad (5)$$

where N_0 is the number of samples of the selected homogenous region from which h_{opt}^0 is estimated and N is the number of sample in the clutter region of the reference window.

It is worth mentioning that when we transform the fitted distribution in the log-intensity domain back to the intensity domain, the PDF becomes the sum of lognormal distributions:

$$\hat{f}_I(x) = \frac{1}{N} \sum_{i=1}^N \left\{ \frac{1}{\sqrt{2\pi}hx} e^{-\frac{(\ln x - \ln I_i)^2}{2h^2}} \right\}, \quad (6)$$

where I_1, I_2, \dots, I_N are the clutter samples in the intensity domain. The corresponding CDF is given by:

$$\hat{F}_I(x) = \frac{1}{N} \sum_{i=1}^N \Phi\left(\frac{\ln x - \ln I_i}{h}\right), \quad (7)$$

where $\Phi(x)$ is the CDF of the standard normal distribution. Equation (6) and Equation (7) indicate that using the KDE in the log-intensity domain with the Gaussian kernel function is in fact to fit a simple lognormal mixture model (LMM) in the intensity domain. This may in turn inspire us to use a finite LMM in the intensity domain or to equivalently use a standard finite Gaussian mixture model (GMM) in the log-intensity domain with the expectation-maximization (EM) algorithm [16]. However, one major drawback of this approach is the significantly increased computational load. Local implementation for CFAR detection can be very slow because estimating the model parameters requires extensive iteration. On the other hand, the KDE in the log-intensity domain does not require any adaptive parameter estimation and the distribution can be readily fitted.

C. Effects of Sample Dependency

So far in Section II-A and Section II-B, the use of the KDE has been presented based on the implicit assumption that the samples drawn from the clutter region are independent with each other. Particularly, the optimal kernel bandwidths in Equation (2) and Equation (4) rely on the independency of samples. However, in more realistic cases, the pixels are spatially correlated due to oversampling of the data [15]. Thus estimating the marginal PDF by the KDE with correlated samples drawn from a stationary process deserves further justification.

Following the reference of [10], we note that the asymptotically optimal kernel bandwidths in

Equation (2) and Equation (4) still hold for correlated samples, as long as the process is *short-range* dependent. Short-range dependency says that the sum of the correlation function is bounded, *i.e.*,

$$\sum_x \sum_y \rho(x, y) < \infty, \quad (8)$$

where $\rho(x, y)$ is the spatial correlation function of the stationary process. For the SAR data, this correlation function can be approximately modeled by [15]:

$$\rho(x, y) = \text{sinc}\left(\frac{x}{l_x}\right) \text{sinc}\left(\frac{y}{l_y}\right), \quad (9)$$

where $\text{sinc}(x) = \frac{\sin(\pi x)}{\pi x}$; l_x and l_y are the correlation length in both x and y directions. It can be verified that $\rho(x, y)$ defined by Equation (9) satisfies the short-range dependent condition. This legitimates the use of Equations (2) and (4) as optimal kernel bandwidths even for correlated clutter samples.

Nevertheless, the optimality of Equations (2) and (4) is only in an asymptotic sense. Correlation among samples does introduce discrepancy, especially for single-look SAR image data with high oversampling rate. In this case, we perform multilooking by averaging non-overlapping pixel blocks (*e.g.*, 2×2) to alleviate the spatial dependency as suggested in [15]. For target detection purposes, in particular, it has an extra advantage to reduce the speckle level and improve the signal-to-noise ratio (SCR). However, it should be noted that by spatial multilooking, we do not aim to completely eliminate the pixel correlation. It only serves to improve the estimation accuracy of the marginal distribution. The remaining spatial dependency can be further accounted for as will be addressed in Section III.

D. Fitting Performances

In this part, fitting performances are evaluated with simulated samples generated from a K distribution [15] with the following parameter setting: $L = 3$ (number of looks), $\nu = 6$ (shape parameter), and $\mu = 1$ (distribution mean). We assess the KDE in the intensity domain, the amplitude domain, and the log-intensity domain. In addition, two more typical nonparametric methods, the SVM-based method [17] and the GMM with the EM algorithm [16] are also applied in the log-intensity domain for comparison. For the SVM-based method, the linear programming approach with a dictionary of four radial basis functions [17] is reproduced. For the GMM method, a three-component mixture Gaussian function is fitted.

Three goodness-of-fit (GoF) measures are adopted which are the Kolmogorov-Smirnov (K-S) distance [18], the Anderson-Darling (A-D) distance [19], and the Kullback-Leibler (K-L) distance [14]. Respective formulae for the three distances are given in Table I where $\hat{p}(x)$ or $\hat{F}(x)$ denote the fitted PDF or CDF and $p(x)$ or $F(x)$ denotes the true PDF or CDF which is of the K distribution in our case.

In Table II, the averaged GoF distances (as in 100 independent experiments) between the true K distribution and its fitted versions with $N = 100$ independent samples are given. It reveals that using the GMM in the log-intensity domain achieves the highest fitting scores followed by using the KDE in the log-intensity domain. On the other hand, the KDE performs better in the log-intensity domain than in the other two domains (intensity and amplitude). This is especially evident from the A-D and K-L distances which place more weight on the distribution tail that is of particular interest in target detection

purposes. The tail differences are also clear from Fig. 2 where the fitted CDFs are plotted. It can be seen that using the GMM and KDE in the log-intensity domain result in excellent heavy-tail capturing capabilities, whereas using the KDE in both the intensity and amplitude domains show varying degrees of premature behaviors with the amplitude domain suffering less due to the reduced dynamic range.

Furthermore, the fitting performance is also evaluated with dependent samples. For simplicity, dependent samples are drawn from a one-dimensional correlated process with a K marginal distribution. Following the procedure proposed in [20], this correlated K process is generated by multiplying two correlated Gamma processes. Generation of each correlated Gamma process follows a standard multilooking concept. Specifically, a white complex Gaussian noise of zero mean is fed to a linear filter and the output becomes a correlated Gaussian process. Then square envelopes of several such correlated Gaussian processes are averaged to produce the correlated Gamma process. The flowchart of generating the correlated K process is shown in Fig. 3 in which the symbols respectively denote:

- $\varepsilon_i[n], \zeta_i[n]$: complex white Gaussian noise with zero mean;
- $h[n]$: impulse response of the linear system;
- $x[n], y[n]$: correlated Gamma process;
- $z[n]$: correlated K process.

Especially, $z[n]$ is controlled so that it has exactly the same marginal distribution to the previous independent case ($L = 3, \nu = 6, \mu = 1$) and the correlation function of $z[n]$ is shown in Fig. 4 from which we can see the introduced dependency. In Table III, the averaged GoF distances between the true marginal distribution and its fitted versions with $N = 100$ dependent samples are given. Compared

with the results in Table II, fitting accuracy has been generally decreased, not surprisingly. Such performance degradation is mainly due to the reduction in the equivalent number of independent samples which is intrinsic in using correlated samples. According to [21], the equivalent number of independent samples from a correlated process can be approximated by:

$$N_e = \frac{1 - \rho}{1 + \rho} \cdot N, \quad (10)$$

where ρ is the lag-1 correlation coefficient. Then using N dependent samples is in fact equivalent to using N_e (smaller than N) independent samples and so the accuracy is bound to diminish as observed in Table III by each and every method.

One last comment is on the computational efficiency. Although using the GMM in the log-intensity domain has shown inspiring clutter estimation performances, it becomes less attractive for adaptive implementation because of the time-consuming parameter learning. The SVM-based method suffers even more severely because the fitting requires solving a large scale linear programming problem [17]. In view of both fitting efficiency and accuracy, using the KDE in the log-intensity turns out to offer the best trade-off among different nonparametric estimation approaches.

III. CORRELATION STRUCTURE MODELING USING COPULA

A. Definition

In this section, it is assumed that the marginal distribution of the test samples $\mathbf{X} = (X_1, X_2, \dots, X_d)^T$ within the test region of the reference window is known (estimated) and the focus now is to characterize the correlation structure embedded in them. Denote the marginal CDF by $F(x)$

and we do the following transformation:

$$U_i = F(X_i), i = 1, 2, \dots, d. \quad (11)$$

The basic reasoning on performing the above transformation is that by doing so U_i will become a uniformly distributed random variable. As a result, the transformed random vector $\mathbf{U} = (U_1, U_2, \dots, U_d)^T$ will be independent of any specific marginal distribution forms and its joint distribution only reflects the correlation structure of $\mathbf{X} = (X_1, X_2, \dots, X_d)^T$. In statistics, such a relationship is usually called a copula [11]. Specifically, the copula of \mathbf{X} is defined as the joint CDF of \mathbf{U} , that is:

$$C(u_1, u_2, \dots, u_d) = P\{U_1 \leq u_1, U_2 \leq u_2, \dots, U_d \leq u_d\}. \quad (12)$$

The theory of copula states that the joint CDF of \mathbf{X} can be completely characterized by its marginal CDF and copula, thanks to Sklar's theorem [11], *i.e.*,

$$F(x_1, x_2, \dots, x_d) = P\{X_1 \leq x_1, X_2 \leq x_2, \dots, X_d \leq x_d\} = C(F(x_1), F(x_2), \dots, F(x_d)), \quad (13)$$

where $F(x_1, x_2, \dots, x_d)$ is the joint CDF of \mathbf{X} and $F(x)$ is the marginal CDF. Equation (13) indicates that in order to characterize the joint distribution of \mathbf{X} , all we have to do is to find its underlying copula if the marginal CDF is known or can be estimated as in our case. One may refer to [11] for a more detailed description of the copula as well its application.

B. Parameter Estimation

Particularly in the subject matter of this paper, our purpose is to exploit the spatial correlation underlying the pixel block $\mathbf{X} = (X_1, X_2, \dots, X_d)^T$ in the test region of the reference window, which is nothing but to estimate the copula for \mathbf{X} . More importantly, such a task is greatly facilitated by the fact that this underlying copula can be considered spatially invariant over the entire image if the SAR

system PSF is considered mainly responsible for the pixel correlation. Thus we are exempt from having to perform the local estimation but instead, the same homogeneous clutter region may be used again from which the copula of interest can be reliably estimated. For example, in order to estimate the copula for a 3×3 pixel block (*i.e.*, the dimension of the test region is 3×3), we can randomly select M blocks from the homogeneous region and vectorize them to training vectors.

The copula estimation can be implemented both parametrically and nonparametrically. The former is to give the copula a parametric form and copula estimation equally amounts to parameter estimation. The later is to use nonparametric tools such as the KDE to directly estimate the joint density (note that by definition the copula is a joint distribution as well). In this paper, we choose the parametric method, and in particular, the Gaussian copula to model the correlation structure. There are several reasons for this choice. The Gaussian copula offers an analytically tractable way for deriving the detection threshold, whereas the nonparametric copula is generally intractable because the distribution of the test statistic is hard to determine due to its complicated forms. In addition, the histogram in the log-intensity domain resembles a Gaussian shape which makes a Gaussian copula more suitable to other parametric copulas such as the Student-t copula. One more advantage of the Gaussian copula is that the parametric estimation is extremely easy. By definition, the Gaussian copula with a parameter matrix Σ can be written as [11]:

$$C(u_1, u_2, \dots, u_d) = \Phi_{\Sigma}(\Phi^{-1}(u_1), \Phi^{-1}(u_2), \dots, \Phi^{-1}(u_d)), \quad (14)$$

where $\Phi^{-1}(u)$ is the inverse function of the standard normal CDF and $\Phi_{\Sigma}(x_1, x_2, \dots, x_d)$ is the joint normal CDF with zero mean vector and covariance matrix Σ . Equation (14) indicates if $\mathbf{U} = (U_1, U_2, \dots, U_d)^T$ belongs to a Gaussian copula, then the transformed random vector

$\mathbf{Y} = (\Phi^{-1}(U_1), \Phi^{-1}(U_2), \dots, \Phi^{-1}(U_d))^T$ is jointly Gaussian distributed with zero mean and covariance matrix Σ . Consequently, for a random vector $\mathbf{X} = (X_1, X_2, \dots, X_d)^T$ subject to marginal distribution $F(x)$ and Gaussian copula, it can be turned into a Gaussian vector \mathbf{Y} by the following transformation:

$$\mathbf{Y} = \begin{pmatrix} Y_1 \\ Y_2 \\ \vdots \\ Y_d \end{pmatrix} = \begin{pmatrix} \Phi^{-1}(F(X_1)) \\ \Phi^{-1}(F(X_2)) \\ \vdots \\ \Phi^{-1}(F(X_d)) \end{pmatrix}, \quad (15)$$

where the joint PDF of \mathbf{Y} is multivariate Gaussian:

$$p(\mathbf{y}) = \frac{1}{(2\pi)^{\frac{d}{2}} |\Sigma|^{\frac{1}{2}}} \exp\left(-\frac{1}{2} \mathbf{y}^T \Sigma^{-1} \mathbf{y}\right), \quad (16)$$

Then suppose for parameter estimation M training vectors $\mathbf{X}_1, \mathbf{X}_2, \dots, \mathbf{X}_M$ are available, we first transform them into $\mathbf{Y}_1, \mathbf{Y}_2, \dots, \mathbf{Y}_M$ according to Equation (15) and the covariance matrix for the Gaussian copula can be straightforwardly estimated by:

$$\hat{\Sigma} = \frac{1}{M} \sum_{m=1}^M \mathbf{Y}_m \mathbf{Y}_m^T. \quad (17)$$

C. Validation of the Gaussian Copula Model

In this sub-section, we provide numerical validation of using the Gaussian copula to model the underlying correlation structure for both simulated and real SAR clutter. The basic evaluation principle lies in the fact under the Gaussian copula assumption, the transformed vector \mathbf{Y} given by Equation (15) will conform to the joint Gaussian distribution such that a test of multivariate normality can be applied. Particularly, if \mathbf{Y} is indeed jointly Gaussian with zero mean and covariance matrix Σ , then the following test statistic will have a chi-squared distribution with d degrees of freedom:

$$\Lambda = \mathbf{Y}^T \Sigma^{-1} \mathbf{Y}. \quad (18)$$

Thus we can calculate the GoF of the chi-squared distribution for Λ to indicate the normality of Y .

Based on the above reasoning, we first evaluate using the Gaussian copula to characterize the underlying correlation structure for a 2-dimensional correlated K clutter. The marginal distribution is controlled such that $L = 3, \nu = 6, \mu = 1$ and the correlation functions in both the vertical and horizontal directions are shown in Fig. 5. Particularly we investigate the joint distribution among 3×3 pixel blocks. We randomly select 1000 such blocks from the correlated process and construct their corresponding sample vectors $\mathbf{X}_i (i = 1, 2, \dots, 1000)$. Since our primary concern is the correlation structure, the exact marginal CDF of the K distribution [22] is used to transform \mathbf{X}_i to \mathbf{Y}_i according to Equation (15). Then Equation (17) is used to estimate the covariance matrix and finally the test statistics Λ_i are computed by Equation (18). In Fig. 6 we plot the empirical CDF of Λ_i and its predicted theoretical distribution (*i.e.*, chi-squared distribution with $d = 9$ degrees of freedom). It can be seen that a well consistent result has been obtained. In addition, the p-value for hypothesizing Λ_i to the chi-squared distribution by the K-S test is as high as 0.9743, which confirms the validity of correlation modeling with the Gaussian copula.

Next we test Gaussian copula modeling for real SAR data. Fig. 7 shows a 150×150 homogenous sea clutter area selected from an ALOS-PALSAR image. Its correlation functions in both horizontal and vertical directions are displayed in Fig. 8. The evaluation procedure is basically the same to the simulated example except that now the marginal CDF is estimated by the KDE in the log-intensity domain with all the available clutter samples. In Fig. 9 we plot the empirical CDF of Λ_i together with its predicted theoretical distribution. The K-S test also gives a p-value as high as 0.9158, which

validates the usability of Gaussian copula for real SAR clutter as well.

D. Test Statistic Construction

As a consequence of applying the Gaussian copula, for any random vector $\mathbf{X} = (X_1, X_2, \dots, X_d)^T$ under test, its transformed counterpart $\mathbf{Y} = (Y_1, Y_2, \dots, Y_d)^T$ by Equation (15) will be jointly Gaussian with the PDF given in Equation (16). Thus a simple likelihood test statistic becomes nothing but the quadratic detector, that is, $\Lambda = \mathbf{Y}^T \Sigma^{-1} \mathbf{Y} > \gamma$. It is interesting to note that this detector is very similar to the spatial whitening filter (SWF) [23]. The difference is that the SWF is applicable in the complex SAR imagery whereas our method processes detected (real) SAR images. In addition, according to Section III-C, $\Lambda = \mathbf{Y}^T \Sigma^{-1} \mathbf{Y}$ conforms to the chi-squared distribution with d degrees of freedom under the null hypothesis, from which the detection threshold γ corresponding to a given probability of false alarm (PFA) can be easily determined.

Note, however, that the simple quadratic detector can be further improved by taking the target of interest into account. For ship detection in SAR images, what we are interested are “light” blobs or pixel blocks with large intensity values. Thus a modified version can be written as:

$$\Lambda_M = \chi \left(\sum_{i=1}^d Y_i \right) \cdot \mathbf{Y}^T \Sigma^{-1} \mathbf{Y} > \gamma, \quad (19)$$

where the $\chi(t)$ denotes the step function with $\chi(t) = 1$ if $t > 0$ and $\chi(t) = 0$ otherwise. By symmetry, the threshold γ in Equation (19) for a given PFA is the same to that in $\mathbf{Y}^T \Sigma^{-1} \mathbf{Y} > \gamma$ for the PFA that is twice larger.

In passing, we mention that the detector can be simply designed on a single-point basis without

incorporating the correlation information, which corresponds to the test region consisting of only one pixel. In this case the marginal distribution is all that is needed and the test statistic becomes:

$$\Lambda_S = F(X) > \gamma, \quad (20)$$

where X is the pixel value under test and $F(x)$ is the marginal CDF. Note that Λ_S obeys the uniform distribution on $[0,1]$ so that the detection threshold can be straightforwardly set to be $\gamma = 1 - P_0$ where P_0 is the required PFA.

IV. CFAR SHIP DETECTION ALGORITHM

In this section, we sum up the CFAR ship detection algorithm according to Section II and Section III for implementation convenience. The processing chain is as follows.

- **Step 1: System Setup**

- 1) Determine the appropriate configuration for the moving reference window including the size of the test region, the guard region as well as the clutter region.
- 2) Set the PFA P_0 and determine the detection threshold γ based on the null distribution (chi-squared) of the detector.

- **Step 2: Preprocessing**

- 1) If the SAR image is single-look, perform spatial multilook processing by combining (averaging) non-overlapping image blocks in the intensity domain; if the SAR image is already multilook processed, this step is optional.
- 2) Transform the SAR intensity data into the log-intensity domain.

- **Step 3: Parameter Estimation**

- 1) Select a homogeneous region from the SAR image.
- 2) Estimate the initial kernel bandwidth h_{opt}^0 from the selected homogeneous region by the plug-in method (*e.g.*, [24]) and rescale the kernel bandwidth to h_{opt} by Equation (5).
- 3) Randomly select M image blocks (of the same shape to the test region of the reference window) from the homogenous region and construct M training vectors $\mathbf{X}_1, \mathbf{X}_2, \dots, \mathbf{X}_M$; then transform $\mathbf{X}_1, \mathbf{X}_2, \dots, \mathbf{X}_M$ into $\mathbf{Y}_1, \mathbf{Y}_2, \dots, \mathbf{Y}_M$ by Equation (15) and subsequently estimate the covariance matrix Σ by Equation (17).

● **Step 4: Adaptive Detection**

- 1) Move the reference window over the image and at each position estimate the local marginal CDF $\hat{F}(x)$ by KDE with the samples from the clutter region; transform the central pixel value X to Y by $Y = \Phi^{-1}(\hat{F}(X))$.
- 2) For each position in the transformed image, construct the test vector \mathbf{Y} in the test region and calculate the test statistic according to Equation (19); label the central pixel as target if it is larger than the detection threshold γ .

V. EXPERIMENTS

A. Simulation Analysis

The basic simulation scenario is a 1000×1000 image contaminated by a correlated K clutter. The marginal distribution is also controlled at $L = 3, \nu = 6, \mu = 1$ and the correlation functions in both the vertical and horizontal directions are the same to those in Fig. 5. The proposed modified quadratic detector (MQD) uses a 41×41 reference window with a 3×3 test region and 31×31 guard region. At

each position, the test statistic is calculated by Equation (19) for the null hypothesis where only clutter samples are present. Then the test statistic is re-calculated for the alternative hypothesis where the pixels in the test region are replaced by random target samples of Gamma distribution [15] with $L = 3$ and $\mu = 2$. In this way, a receiver operating characteristic (ROC) curve can be generated. In addition, the ROC curves of the single-point detector (SPD) with the marginal CDF estimated by different methods are also generated. Specifically, the marginal CDF is respectively estimated by the KDE in three domains (log-intensity, amplitude, intensity) and the GMM in the log-intensity domain. The SVM-based approach is not included in the comparison because it is too slow to be applicable in the adaptive scenario. All the ROC curves are drawn together in Fig. 10. Not surprisingly, the MQD significantly outperforms the other SPDs by jointly testing multiple pixels. In addition, note that the SPDs almost have the same ROC curves. Their distinction, however, resides in the different false alarm rate (FAR) control abilities which reveal the relationship between the false alarm occurrence (true PFA) and the predetermined PFA. Ideally, identity relation is expected but in practice deviation will happen due to the errors of the estimated distribution. As can be seen in Fig. 11, the most accurate result is achieved by the SPD using GMM and KDE in the log-intensity domain. Performance degradation is observed for the MQD. This should have been expected since the accuracy for fitting a higher dimensional distribution will be inevitably decreased due to the increased uncertainty. Still, it should be noted that such accumulated uncertainty mostly comes from estimating the marginal distribution with finite samples whereas we have shown the Gaussian copula can well characterize the correlation structure in Section III-C. Nevertheless, the MQD shows better FAR control ability than the SPDs using KDE in the

amplitude and intensity domains. The latter two detectors all have more severe saturating effect attributed to their insufficiency to resolve heavy-tailed data as revealed by Fig. 2.

The size of the guard region is another factor that affects the detection performance. If the guard region is smaller than the target dimension, target pixels will intrude into the clutter region, resulting in less accurate clutter modeling and subsequently performance degradation. For example, we consider detecting a 15×15 target embedded in the clutter. The target values are assumed to be Gamma distributed with $L = 3$ and $\mu = 10$. Adaptive detection is performed with a 41×41 reference window. In principle, the size of the guard region must be at least twice as large as the target of interest (29×29 in this case). Table IV shows the changes of the detection rate of different detectors with varying guard regions. It should be noted that the values in Table IV does not denote the absolute detection rate but a normalized percentage with regard to the detection rate with a 29×29 guard region. It can be seen that using a smaller guard region leads to reduced detected target pixels for all the detectors but the MQD appears to exhibit a stronger robustness than the SPDs against performance degradation. If we consider the error tolerance as the point where the detection rate is halved, then the MQD allows using a guard region designed for a 10×10 target in this case.

Last, we compare the computing time of different detectors using MATLAB codes and the results are given Table V. The KDE-based SPDs are the quickest. The MQD takes a slightly longer time. The GMM-based SPD, however, is much slower which can be a major disadvantage for its application in adaptive detection systems.

B. Experimental Results with Real SAR Data

The test SAR image acquired by RADARSAT-2 over the Port of Tianjin (China) is used for validation. The format of the original scene is single look complex (SLC). Spatial multilooking is performed by combining 2×2 (azimuth \times range) pixels in the intensity domain. The multilook processed test image is then displayed in Fig. 12(a). Ship detection is conducted with the five aforementioned methods: the MQD, the four SPDs with the marginal CDF respectively estimated by KDE in the three domains (log-intensity, amplitude, intensity) and GMM in the log-intensity domain. It should be noted that for the KDE in the intensity and amplitude domains, adaptive kernel bandwidth is used according to the reasoning in Section II-A. The size of the reference window is 41×41 with a 31×31 guard region. For the MQD, the test region is 3×3 and for the SPD the test region is 1×1 . For all detectors the prescribed PFA is set to be $P_0 = 10^{-8}$ which is required for the Maritime Satellite Surveillance Radar (MSSR) mode of the Canadian RADARSAT program [25]. The detection results are shown in Fig. 12(b)-(f) from which it can be seen that the MQD produces the best outcome in terms of detected target pixels. In addition, particular attention should be paid to the detection result made by the SPD with KDE in the intensity domain. This detector produces a significant number of false alarms even the prescribed PFA is extremely low. Such observation demonstrates again the inability of KDE in the intensity domain to capture heavy-tailed data.

VI. CONCLUSION

In this paper, a semiparametric clutter estimation method for SAR images is proposed. The main contribution of the work consists in two points. First, we systematically evaluated the applicability of

the nonparametric KDE for estimating the marginal distribution of the SAR clutter data and showed that the KDE is mostly appropriate to be applied in the log-intensity domain. Secondly, we proposed to use a parametric copula to characterize the pixel correlation and gave corresponding target detector together with its null distribution for CFAR detection.

In addition, although in this paper a semiparametric approach is adopted, it is also possible to replace the KDE with any known parametric marginal distributions whenever applicable. Separate modeling of the marginal distribution and the correlation structure can thus be considered a general scheme for applications in which estimation of the joint distribution is needed. While in this paper we have particularly applied the Gaussian copula for modeling the joint distribution of spatially correlated clutter in single-channel SAR imagery, interested readers may refer to some other works such as [27] where copulas can be also used for dependency characterization between polarimetric channels.

APPENDIX

In this appendix, we review some key formulae and results of the KDE. Suppose X_1, X_2, \dots, X_N are identically and independently distributed random samples from an unknown probability density function (PDF). The kernel density estimator (KDE) is defined as:

$$\hat{p}(x) = \frac{1}{Nh} \sum_{i=1}^N K\left(\frac{x - X_i}{h}\right), \quad (\text{A1})$$

where $K(x)$ is called the kernel function. Throughout this paper the Gaussian kernel given in (A2) is used because of its simplicity and infinite derivability.

$$K(x) = \frac{1}{\sqrt{2\pi}} \exp\left(-\frac{x^2}{2}\right). \quad (\text{A2})$$

The kernel bandwidth h controls the smoothness of the estimated PDF. Under the criteria of asymptotic mean integrated squared error (AMISE), the optimal bandwidth is [24, 26]:

$$h_{\text{opt}} = \left(\frac{C_1}{C_2^2 AN}\right)^{\frac{1}{5}}, \quad (\text{A3})$$

where N is the number of samples; C_1 , C_2 , and A are constants that are respectively given by:

$$C_1 = \int_{-\infty}^{+\infty} [K(x)]^2 dx, \quad (\text{A4})$$

$$C_2 = \int_{-\infty}^{+\infty} x^2 K(x) dx, \quad (\text{A5})$$

$$A = \int_{-\infty}^{+\infty} [p''(x)]^2 dx. \quad (\text{A6})$$

If the Gaussian kernel in Equation (A2) is used, we have $C_1 = 1/(2\sqrt{\pi})$, $C_2 = 1$. On the other hand the constant A depends on the PDF $p(x)$. This means when the KDE is applied to different domains of the SAR data, different kernel bandwidths should be used. Specifically, in the intensity domain, the pixel value I can be expressed by the product form as in Equation (1). Suppose the PDF of the multiplicative noise is $p_n(x)$, then the PDF of I becomes:

$$p_I(x) = \frac{1}{\sigma} p_n\left(\frac{x}{\sigma}\right). \quad (\text{A7})$$

Substituting (A7) into (A3), the optimal kernel bandwidth for the intensity domain is thus given by Equation (2) in Section II-A.

In the log-intensity domain, the noise model becomes additive, i.e., $\ln I = \ln \sigma + \ln n$. By change of variable, the PDF of $Z = \ln I$ is:

$$p_z(x) = p_n(e^{x-\ln\sigma})e^{x-\ln\sigma}. \quad (\text{A8})$$

Substituting (A8) into (A3), the optimal kernel bandwidth in the log-intensity domain is thus given by Equation (4) in Section II-B.

ACKNOWLEDGEMENT

This work was in part supported by Space Sensing Project funded by the Ministry of Education, Japan, and was in part supported by Selected Research Fund of Tsinghua University. The authors would like to thank the European Space Agency under the Earth Observation Principal Investigator project (project ID: 9175). The authors would also like to thank the Editor, Associate Editor and anonymous reviewers for their constructive comments which significantly elevate the content of this paper.

REFERENCE

- [1] S. Bruschi, S. Lehner, T. Fritz, M. Soccorsi, A. Soloviev, and B. van Schie, "Ship surveillance with TerraSAR-X," *IEEE Trans. on Geosci. Remote Sens.*, vol. 49, no. 3, March 2011.
- [2] J.J. van der Sanden, "Anticipated applications potential of RADARSAT-2 data," *Can. J. Remote Sens.*, vol. 30, no. 3, pp. 369-379, 2004.
- [3] K. Ouchi, "Ship detection by ALOS-PALSAR: an overview," in *Proc. 3rd Int. Conf. APSAR*, Seoul, Korea (South), Sept. 26-30, 2011.
- [4] J. Carretero-Moya, J. Gismero-Menoyo, A. Blanco-del-Campo, A. Asensio-Lopez, "Statistical Analysis of a High-Resolution Sea-Clutter Database," *IEEE Trans. Geosci. Remote Sens.*, vol. 48, no. 4, pp. 2024-2037, Apr. 2010.
- [5] G. Gao, "Statistical modeling of SAR images: a survey," *Sensors*, vol. 10, no. 1, pp. 775-795, 2010.
- [6] A.C. Frery, H.J. Muller, C.C.F. Yanasse, and S.J.S. Sant'Anna, "A Model for Extremely Heterogeneous Clutter," *IEEE Trans. Geosci. Remote Sens.*, vol. 35, no. 3, pp. 648-659, May 1997.
- [7] F. Galland, J.M. Nicolas, H. Sportouche, M. Roche, F. Tupin, P. Refregier, "Unsupervised Synthetic Aperture Radar Image Segmentation Using Fisher Distributions," *IEEE Trans. Geosci. Remote Sens.*, vol. 47, no. 8, pp. 2966-2972, July 2009.
- [8] G. Gao, L. Liu, L. Zhao, G. Shi, and G. Kuang, "An adaptive and fast CFAR algorithm based on automatic censoring for target detection in high-resolution SAR images," *IEEE Trans. Geosci. Remote Sens.*, vol. 47, no. 6, pp. 1685-1697, June 2009.

- [9] J. Ai, X. Qi, W. Yu, Y. Deng, F. Liu, and L. Shi, "A New CFAR Ship Detection Algorithm Based on 2-D Joint Log-Normal Distribution in SAR Images," *IEEE Geosci. Remote Sens. letters*, vol. 7, no. 4, pp. 806-810, Oct. 2010.
- [10] M.P. Wand and M.C. Jones, *Kernel Smoothing*, Chapman & Hall, 1995.
- [11] P.K. Trivedi and D.M. Zimmer, "Copula modeling: an introduction for practitioners," *Foundations and Trends in Econometrics*, vol. 1, no. 1, pp. 1-111, 2005.
- [12] Qingshan Jiang, E. Aitnouri, S. Wang, and D. Ziou. "Automatic Detection for Ship Target in SAR Imagery Using PNN-model," *Can. J. Remote Sens.*, vol. 26, no. 4, pp.297-305, 2000.
- [13] D. J. Crisp, "The state-of-the-art in ship detection in synthetic aperture radar imagery," Intell., Surveillance and Reconnaissance Div., Inf. Sci. Lab., Def., Sci. Technol. Org., Edinburgh, S.A., Australia, Res. Rep. DSTO-RR-0272, May 2004.
- [14] Gui Gao, "A Parzen-Window-Kernel-Based CFAR Algorithm for Ship Detection in SAR Images," *IEEE Geosci. Remote Sens. Letters*, vol. 8, no. 3, pp. 557-561, May 2011.
- [15] C. Oliver and S. Quegan, *Understanding synthetic aperture radar*, SciTech Publishing, Inc., 2004.
- [16] D. Blacknell, "Target detection in correlated SAR clutter," *IEE Proc.-Radar, Sonar, Navig.*, vol. 147, no. 1, pp. 9-16, Feb. 2000.
- [17] J. Weston, A. Gammerman, M.O. Stitson, V. Vapnik, V. Vovk, C. Watkins, "Support vector density estimation," in *Advances in Kernel Methods: Support Vector Learning*, MIT press, Cambridge, MA, 1998.

- [18] M.D. Devore and J.A. O'Sullivan, "Quantitative statistical assessment of conditional models for synthetic aperture radar," *IEEE Trans. Image Process.*, vol. 13, no. 2, pp. 113-125, Feb. 2004.
- [19] T.W. Anderson and D.A. Darling, "A test of goodness of fit," *J. Amer. Stat. Assoc.*, vol. 49, no. 268, pp. 765-769, 1954.
- [20] L.J.Jr. Marier, "Correlated K-distributed clutter generation for radar detection and track," *IEEE Trans. Aerospace Electron. Syst.*, vol. 31, no. 2, pp. 568-580, Apr. 1995.
- [21] F. Zwiers and H. von Storch, "Taking Serial Correlation into Account in Tests of the Mean," *J. Climate*, vol. 8, no. 2, pp. 336-351, Feb. 1995.
- [22] M. Gu and A.A. Douglas, "Using McDaniel's model to represent non-Rayleigh reverberation," *IEEE J. Ocean. Eng.*, vol. 26, no. 3, pp. 348-357, July 2001.
- [23] A. Lopes, J. Bruniquel, F. Sery, J.-C. Souyris and F. Adragna, "Optimal target detection using one channel SAR complex imagery: application to ship detection," in *Proc. IGARSS*, Seattle, USA, Jul. 6-10, 1998.
- [24] Z.I. Botev, J.F. Grotowski and D.P. Kroese, "Kernel Density Estimation via Diffusion," *The Annals Stat.*, vol. 8, no. 5, pp. 2916-2957, 2010.
- [25] C.H. Gierull and I. Sikaneta, "Potential marine moving target indication (MMTI) performance of the RADARSAT constellation mission (RCM)," in *Proc. EUSAR*, Nuremburg, Apr. 23-26, 2012.
- [26] V.C. Raykar and R. Duraiswami, "Fast optimal bandwidth selection for kernel density estimation," *Proc. 6th SIAM Int. Conf. Data Mining*, Bethesda, USA, Apr. 20-22, 2006.

[27] V.A. Krylov, G. Moser, S.B. Serpico, and J. Zerubia, "Supervised high-resolution dual-polarization SAR image classification by finite mixtures and copulas," *IEEE J. Sel. Topics in Sig. Process.*, vol. 5, no. 3, pp. 554-566, June 2011.

Figure Captions:

- Fig. 1 Moving reference window divided into test region (central area), guard region (middle ring) and clutter region (outer ring).
- Fig. 2 Plot of fitted cumulative distribution functions for K distributed samples.
- Fig. 3 Flowchart of correlated K process generation (simulation).
- Fig. 4 Correlation function of 1-D correlated K process.
- Fig. 5 Correlation functions of 2-D correlated K process in (a) horizontal and (b) vertical directions.
- Fig. 6 Plot of empirical CDF of Λ corresponding to 3×3 pixel blocks drawn from 2-D correlated K clutter and theoretical CDF of chi-squared distribution with $d = 9$ degrees of freedom.
- Fig. 7 Intensity display of selected homogeneous sea clutter from ALOS-PALSAR image.
- Fig. 8 Correlation functions of Fig. 7 in (a) horizontal and (b) vertical directions.
- Fig. 9 Plot of empirical CDF of Λ corresponding to 3×3 pixel blocks drawn from Fig.7 and theoretical CDF of chi-squared distribution with $d = 9$ degrees of freedom.
- Fig. 10 Plot of receiver operating characteristic (ROC) curves.
- Fig. 11 Plot of false alarm rate (FAR) control performances.
- Fig. 12 (a) Intensity display of test RADARSAT-2 image and detection results by (b) modified quadratic detector (MQD), (c) single-point detector (SPD) using KDE in the log-intensity domain, (d) SPD using KDE in the amplitude domain, (e) SPD using KDE in the intensity domain, and (f) SPD using GMM in the log-intensity domain. The PFA is all set to be 10^{-8} .

Table Captions:

- TABLE I Formulae of Kolmogrov-Smirnov (K-S), Anderson-Darling (A-D), and Kullback-Leibler (K-L) distances.
- TABLE II Average goodness of fit measures of the fitted distributions with independent samples.
- TABLE III Average goodness of fit measures of the fitted distributions with dependent samples.
- TABLE IV Detection rate changes with varying guard regions. The detection rates are normalized by the detection rate with a 29×29 guard region.
- TABLE V Time consumptions of different detectors using MATLAB codes. The image dimension is 1000×1000 and a 41×41 reference window with a 31×31 guard region is used.

Illustrations:

Figure 1

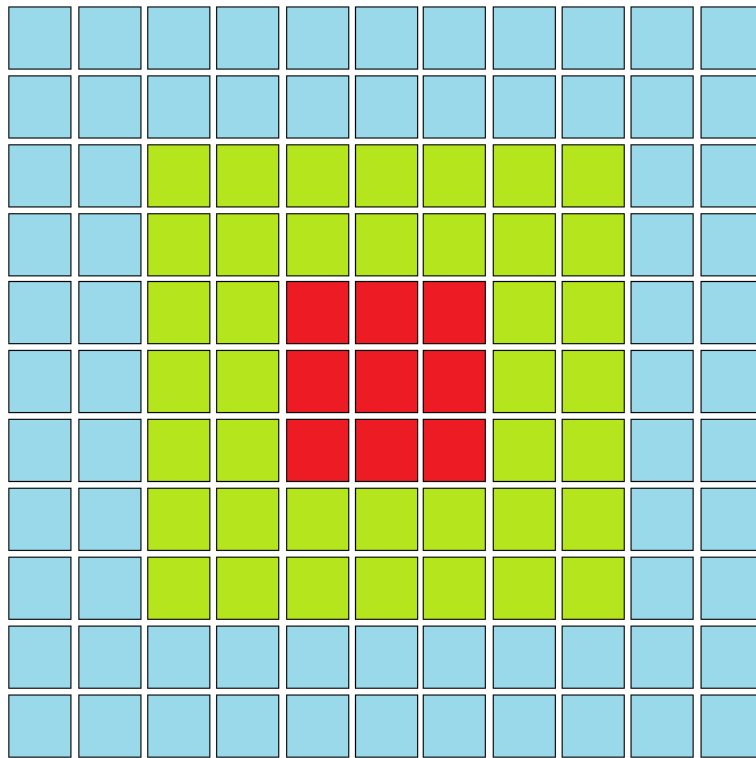


Figure 2

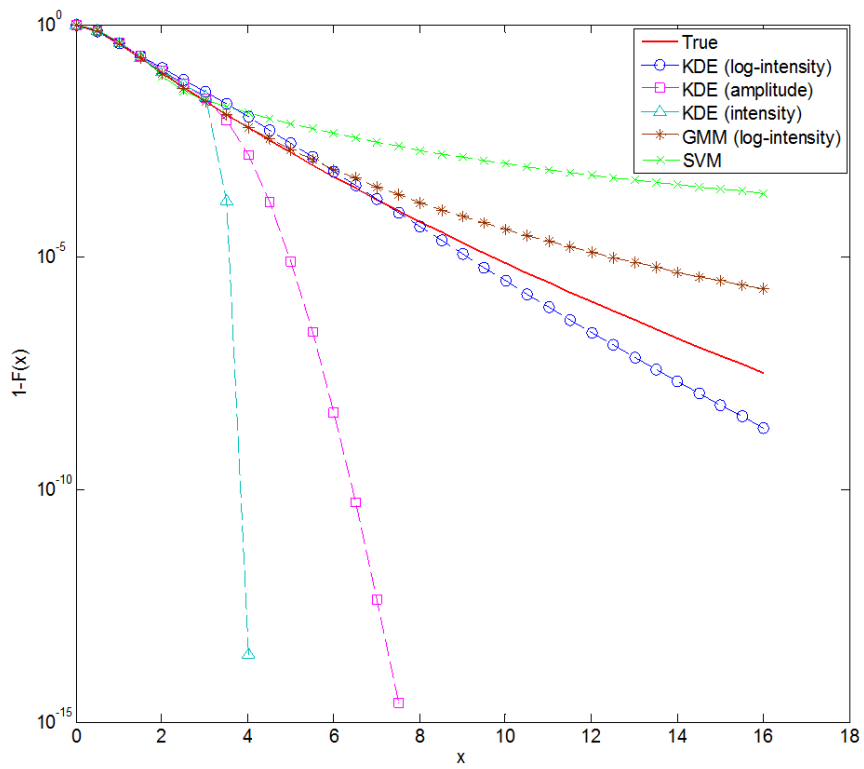


Figure 3

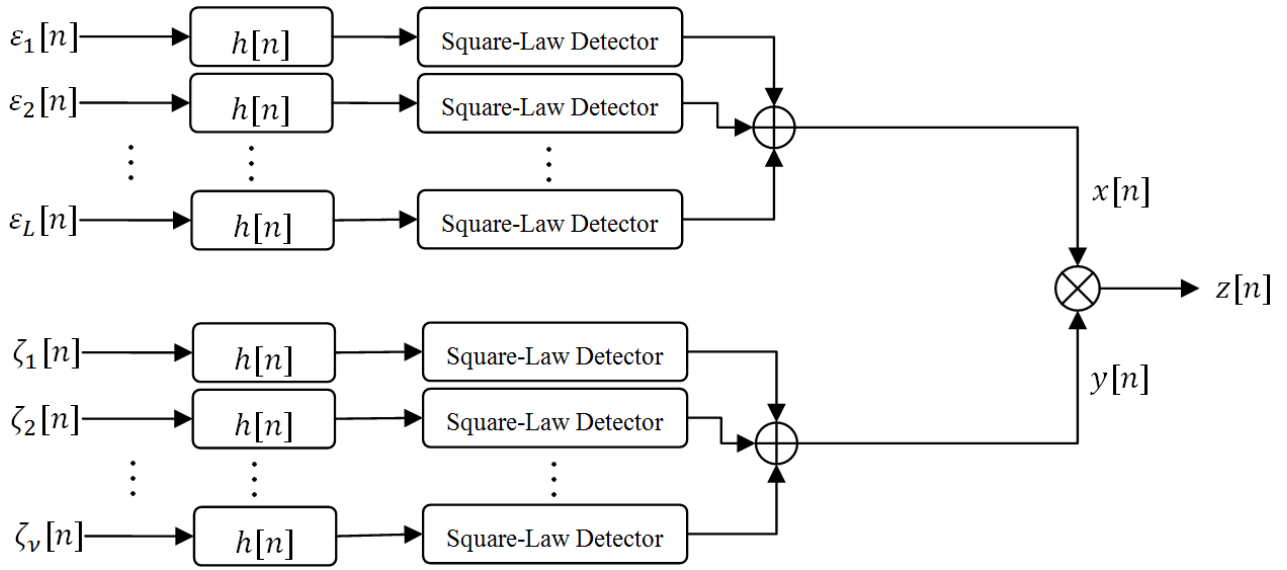


Figure 4

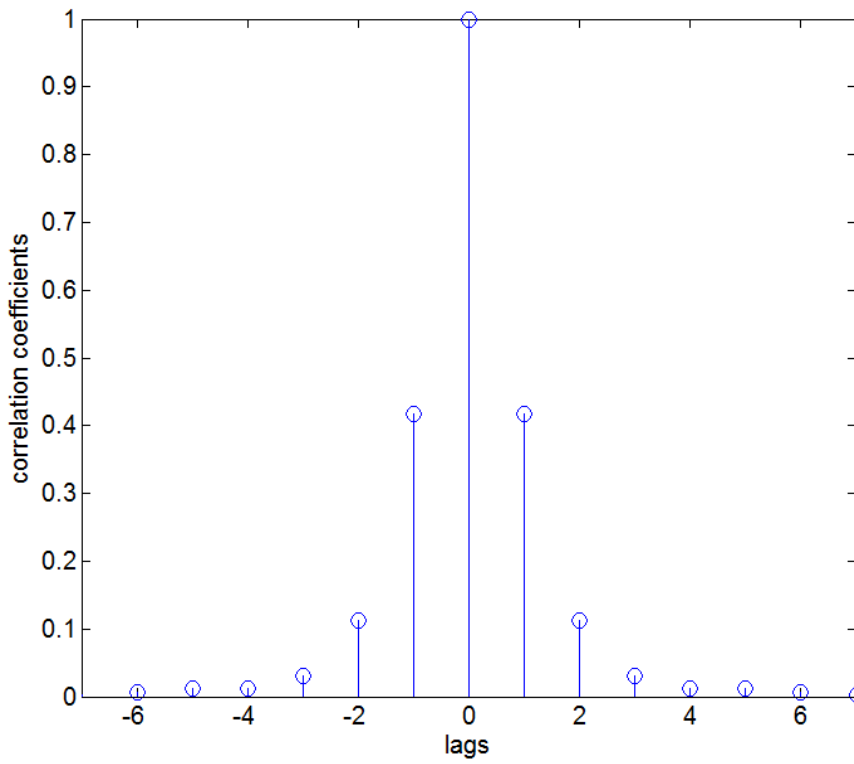
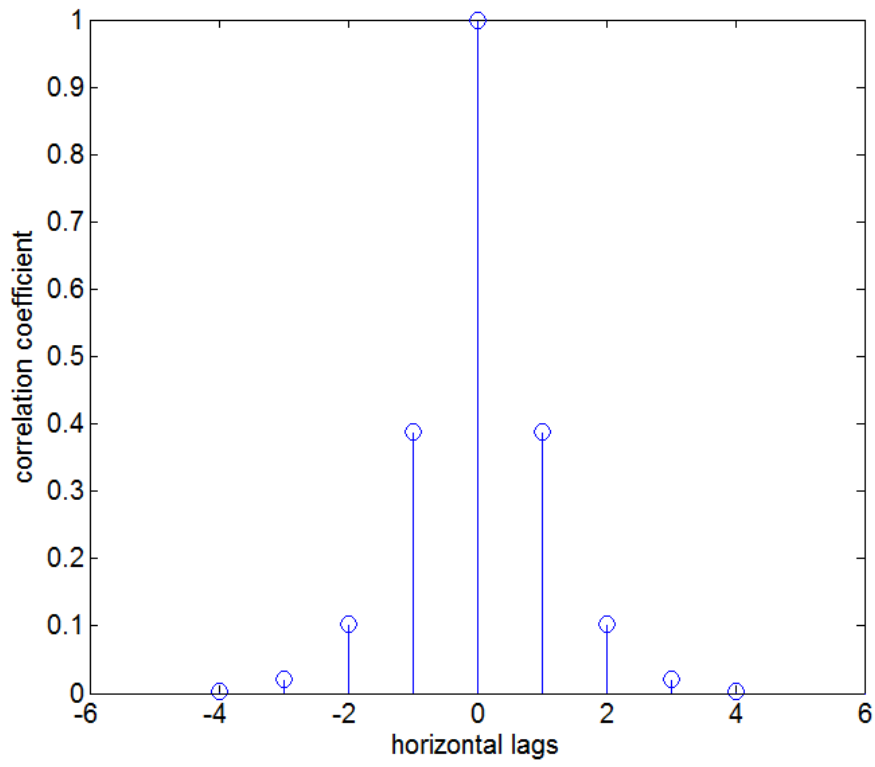
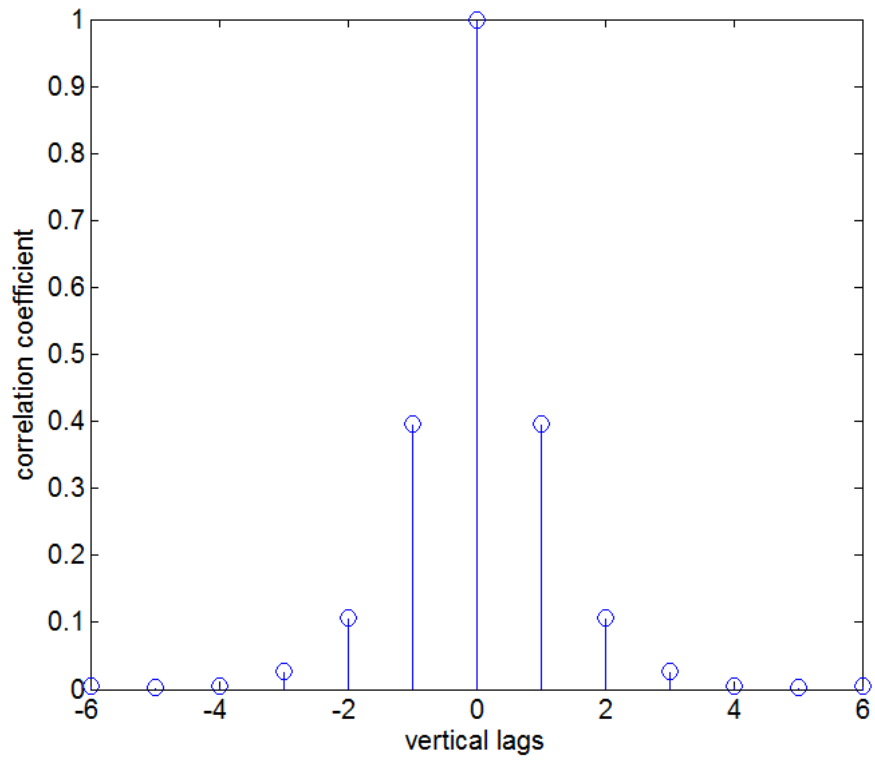


Figure 5



(a)



(b)

Figure 6

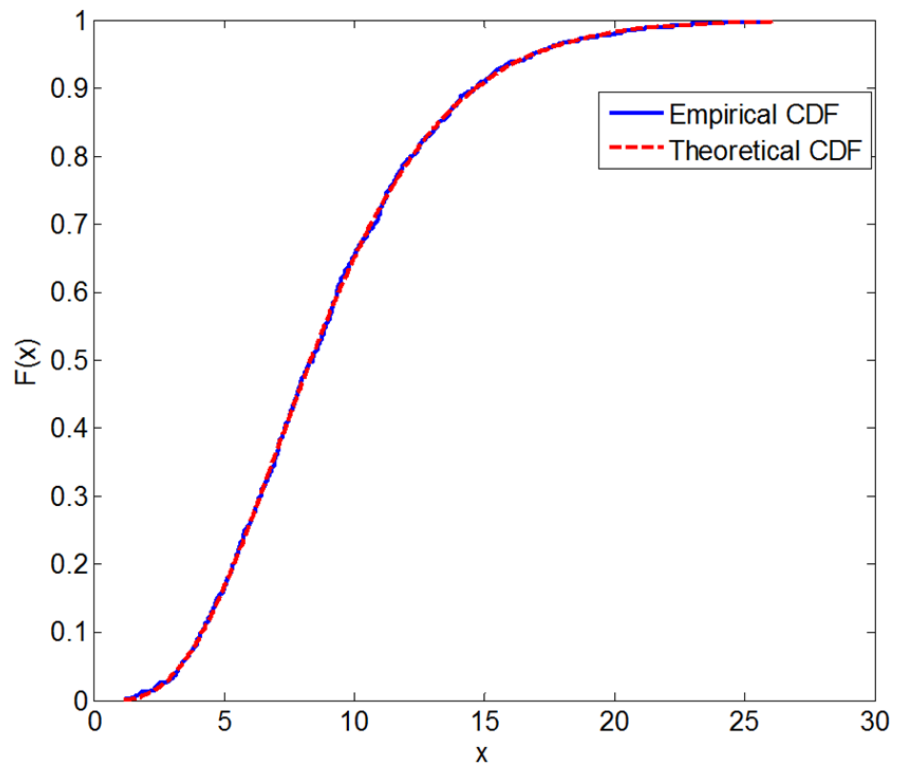


Figure 7

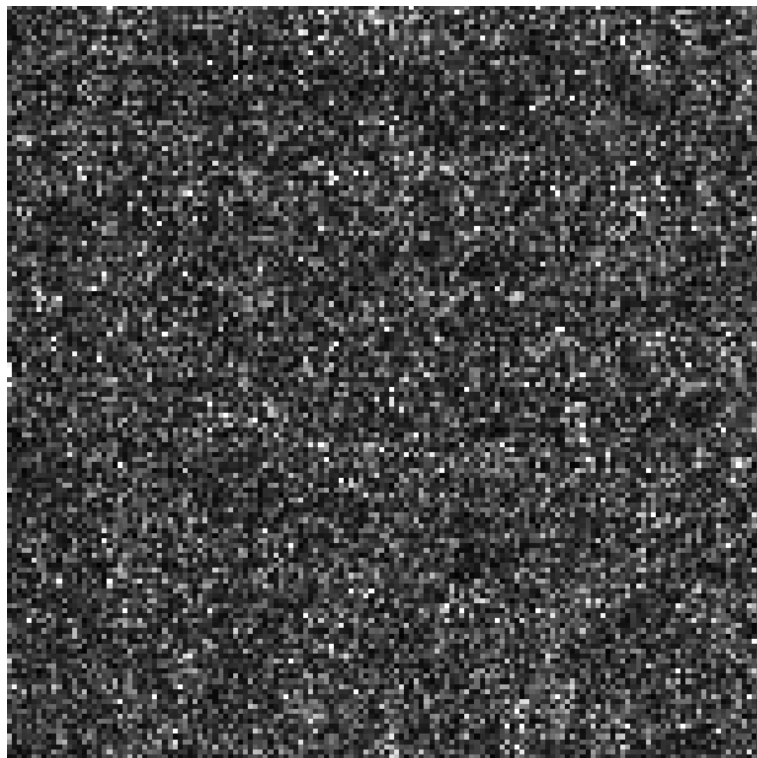
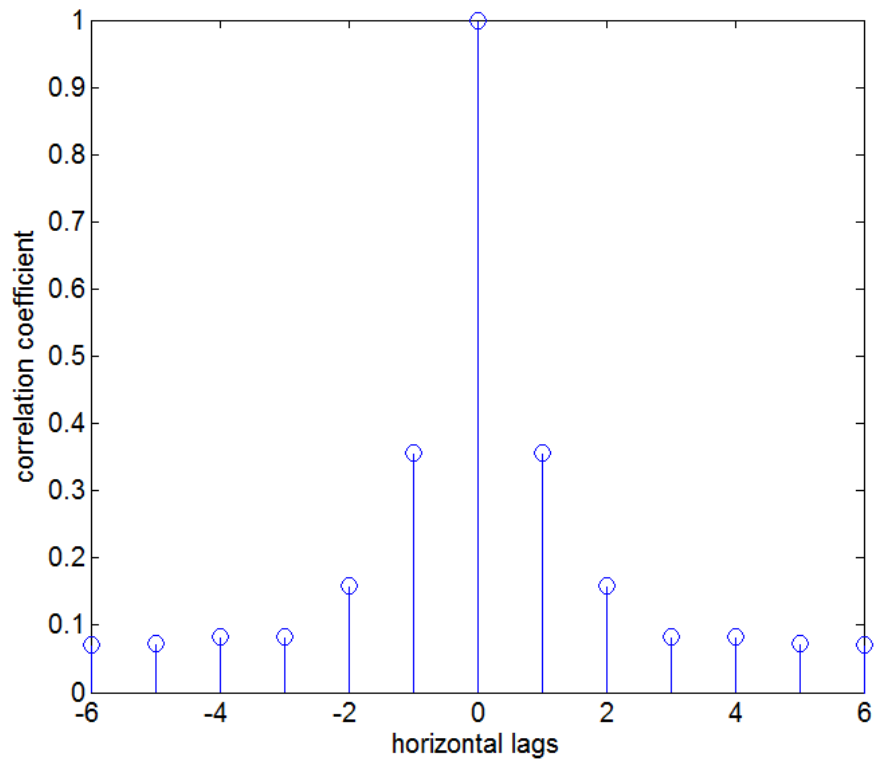
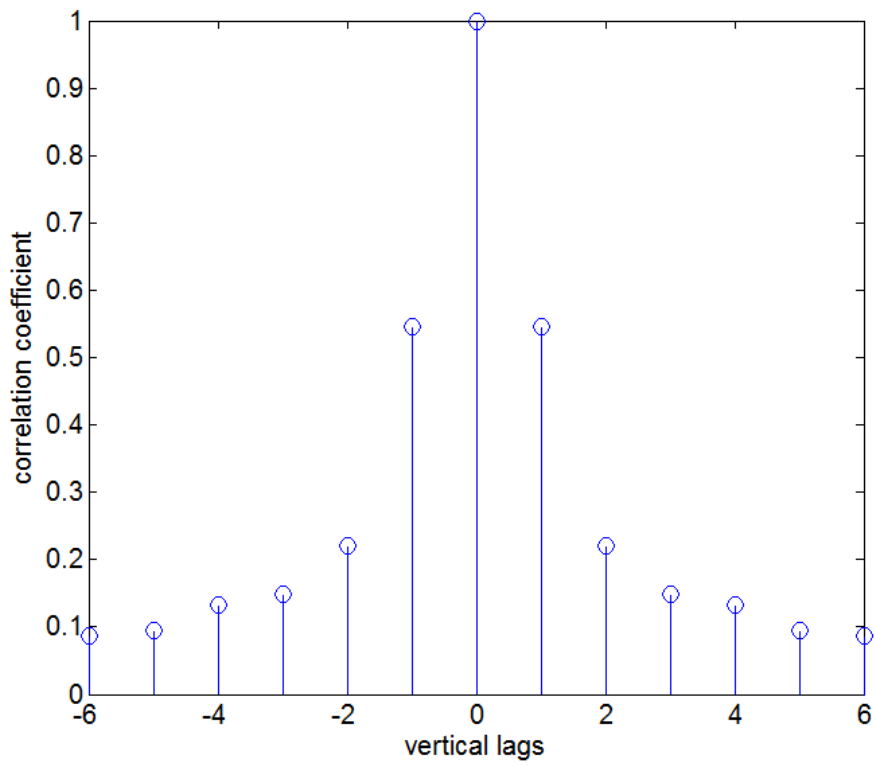


Figure 8



(a)



(b)

Figure 9

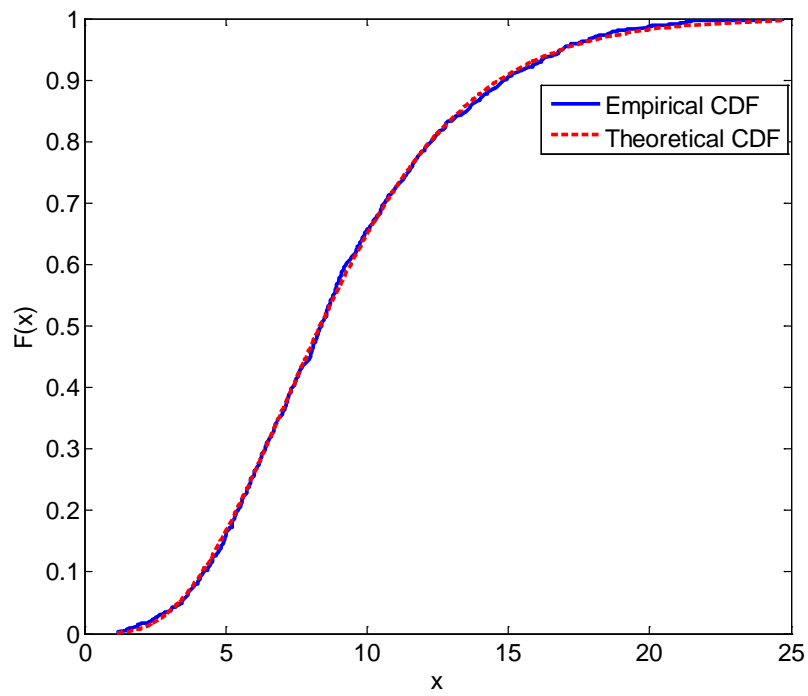


Figure 10

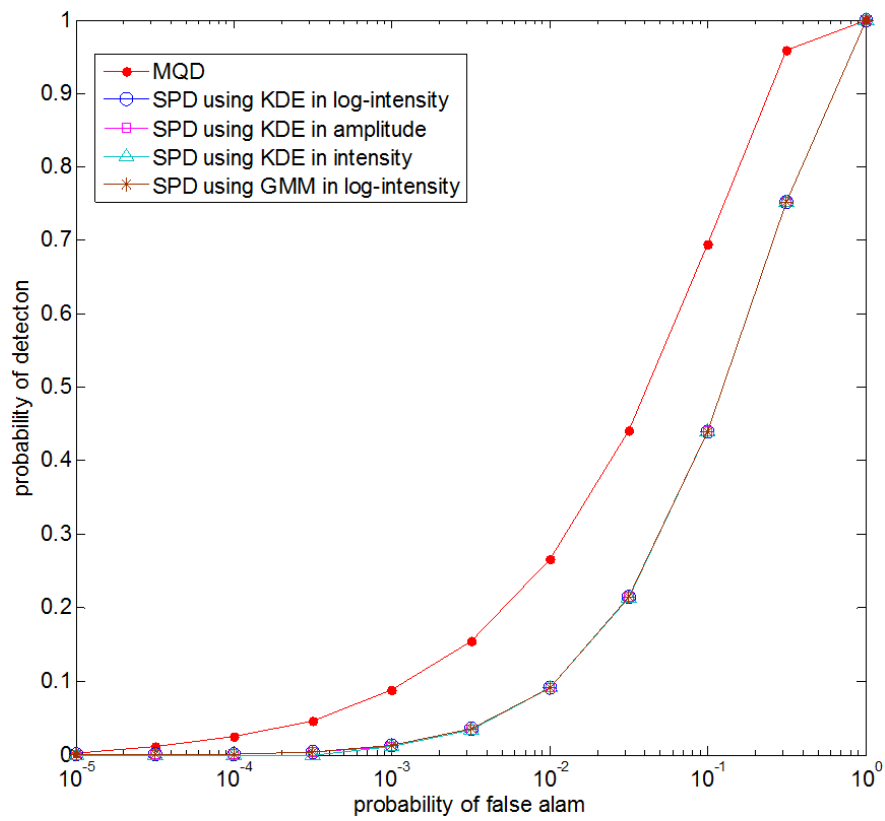


Figure 11

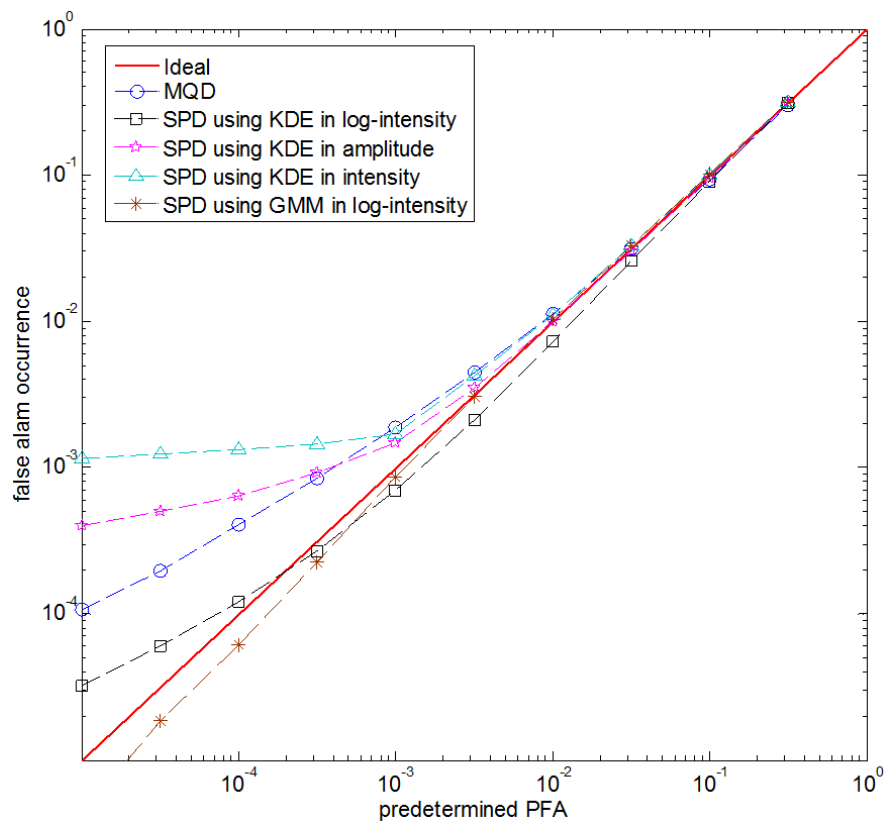
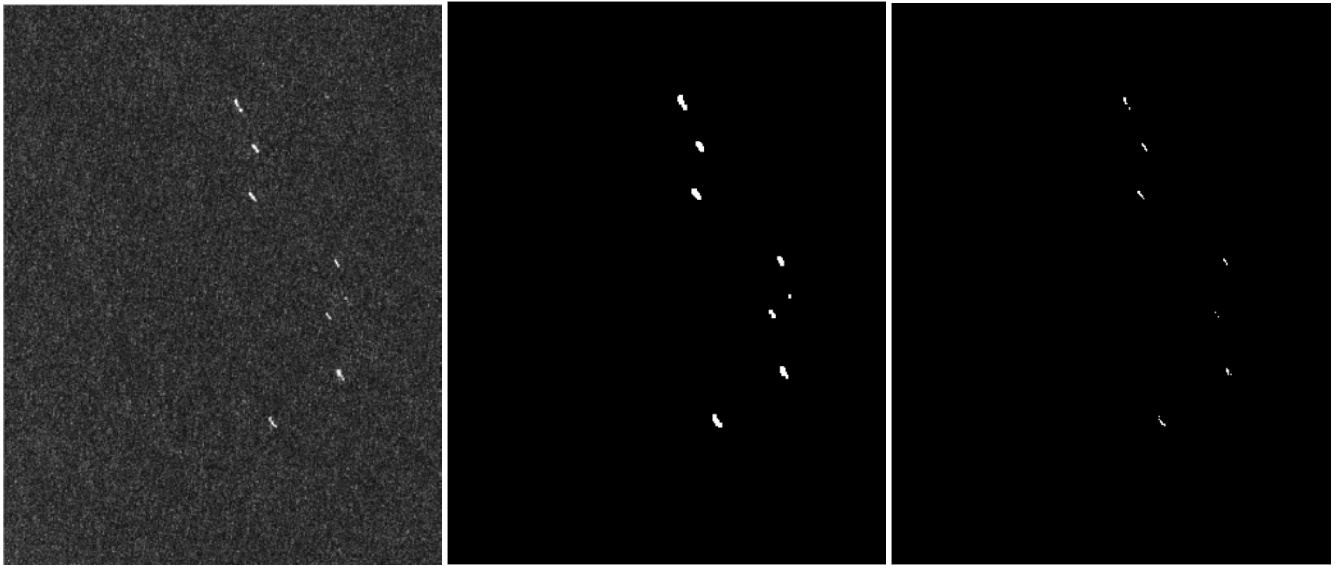


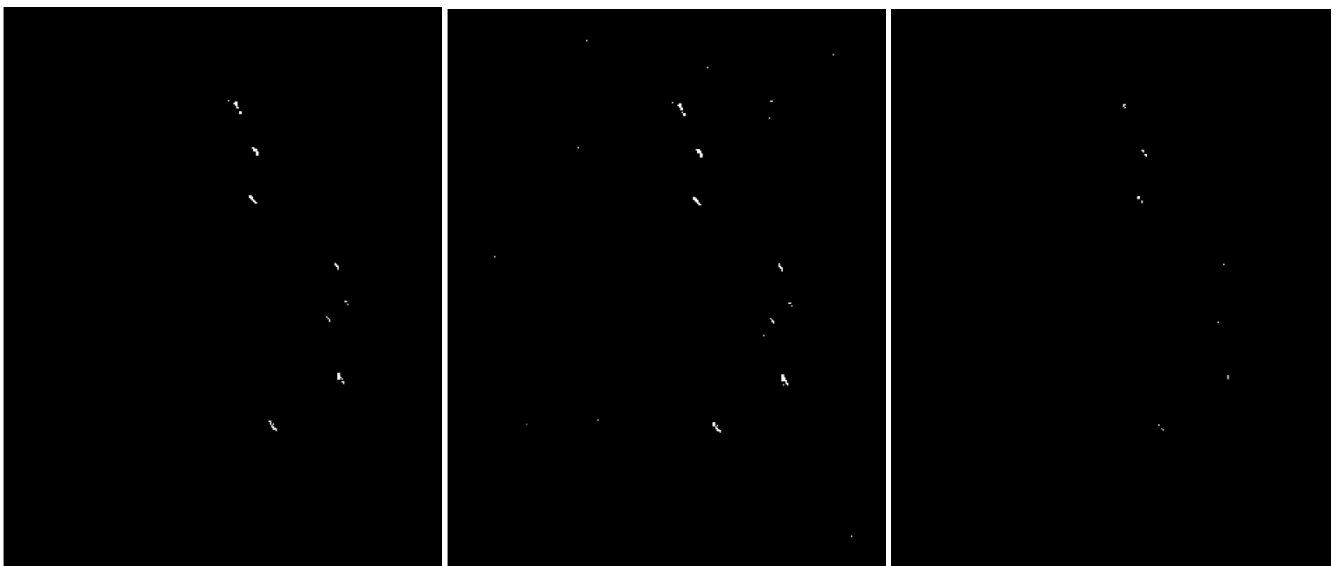
Figure 12



(a)

(b)

(c)



(d)

(e)

(f)

Tables:

TABLE I

FORMULAE OF KOLMOGROV-SMIRNOV (K-S), ANDERSON-DARLING (A-D), AND KULLBACK-LEIBLER

(K-L) DISTANCES

Distances	Formulae
K-S	$D_{KS} = \sup_x F(x) - \hat{F}(x) $
A-D	$D_{AD} = N \int_{-\infty}^{+\infty} \frac{[\hat{F}(x) - F(x)]^2}{F(x)[1 - F(x)]} f(x) dx$
K-L	$D_{KL} = \int_{-\infty}^{+\infty} \hat{f}(x) \ln \frac{\hat{f}(x)}{f(x)} dx$

TABLE II

AVERAGE GOODNESS OF FIT MEASURES OF THE FITTED DISTRIBUTIONS WITH INDEPENDENT SAMPLES

Distances	KDE (LOG ¹)	KDE (AMP ²)	KDE (INT ³)	GMM (LOG ¹)	SVM (LOG ¹)
K-S	0.0478	0.0479	0.0558	0.0489	0.0757
A-D	7.37×10^{-5}	7.68×10^{-5}	7.98×10^{-5}	6.40×10^{-5}	1.19×10^{-4}
K-L	0.0534	0.0689	0.5904	0.0466	0.1970

¹ log-intensity domain

² amplitude domain

³ intensity domain

TABLE III

AVERAGE GOODNESS OF FIT MEASURES OF THE FITTED DISTRIBUTIONS WITH DEPENDENT SAMPLES

Distances	KDE (LOG ¹)	KDE (AMP ²)	KDE (INT ³)	GMM (LOG ¹)	SVM (LOG ¹)
K-S	0.0507	0.0512	0.0589	0.0520	0.0879
A-D	8.43×10^{-5}	8.94×10^{-5}	9.54×10^{-5}	7.96×10^{-5}	1.66×10^{-4}
K-L	0.0536	0.0728	0.6479	0.0500	0.2128

¹ log-intensity domain² amplitude domain³ intensity domain

TABLE IV

DETECTION RATE CHANGES WITH VARYING GUARD REGIONS. THE DETECTION RATES ARE
NORMALIZED BY THE DETECTION RATE WITH A 29×29 GUARD REGION.

Size	MQD ¹	SPD (LOG ²)	SPD (AMP ³)	SPD (INT ⁴)	SPD (GMM ⁵)
29×29	100%	100%	100%	100%	100%
27×27	99.56%	77.52%	76.97%	77.71%	81.55%
25×25	82.22%	60.12%	60.12%	62.28%	61.31%
23×23	62.67%	44.95%	44.95%	46.85%	41.66%
21×21	46.67%	31.46%	32.02%	32.57%	25.59%

¹ modified quadratic detector² single-point detector using KDE in the log-intensity domain³ single-point detector using KDE in the amplitude domain⁴ single-point detector using KDE in the intensity domain⁵ single-point detector using GMM in the log-intensity domain

TABLE V

TIME CONSUMPTIONS (IN SECONDS) OF DIFFERENT DETECTORS USING MATLAB CODES. THE IMAGE DIMENSION IS 1000×1000 AND A 41×41 REFERENCE WINDOW WITH A 31×31 GUARD REGION IS USED.

MQD ¹	SPD (LOG ²)	SPD (AMP ³)	SPD (INT ⁴)	SPD (GMM ⁵)
162 (s)	127 (s)	140 (s)	141 (s)	1856 (s)

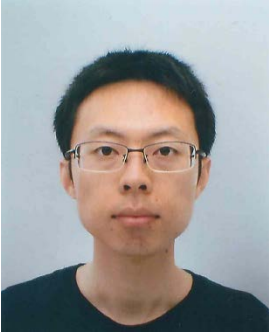
¹ modified quadratic detector

² single-point detector using KDE in the log-intensity domain

³ single-point detector using KDE in the amplitude domain

⁴ single-point detector using KDE in the intensity domain

⁵ single-point detector using GMM in the log-intensity domain



Yi Cui (S'09–M'11) received the B.S. degree (*with honors*) in electronic information science and technology from the College of Electronic Science and Engineering of Jilin University, Changchun, China, in 2006. From 2006 to 2011 he was a doctoral student at Tsinghua University, Beijing, China and received the Ph.D. degree in information and communication engineering from the Department of Electronic Engineering of Tsinghua University in 2011. He is currently a post-doctoral research fellow at Niigata University, Japan.

Dr. Cui is the first-prize winner of the student paper competition at the 2010 Asia-Pacific Radio Science Conference (AP-RASC'10) in Toyama, Japan. His research interests include signal and image processing and their applications in SAR remote sensing, radar polarimetry, and electromagnetic theory.



Jian Yang (M'98–SM'02) received the B.S. and M.S. degrees from Northwestern Polytechnical University, Xian, China, in 1985 and 1990, respectively, and the Ph.D. degree from Niigata University, Niigata, Japan, in 1999.

In 1985, he joined the Department of Applied Mathematics, Northwestern Polytechnical University. From 1999 to 2000, he was an Assistant Professor with Niigata University. In April 2000, he joined the Department of Electronic Engineering, Tsinghua University, Beijing, China, where he is now a Professor.

His interest includes radar polarimetry, remote sensing, mathematical modeling, optimization in engineering, and Fuzzy theory. Dr. Yang is the chairman of IEICE in Beijing area and the vice-chairman of IEEE AES in Beijing chapter.



Yoshio Yamaguchi (M'83–SM'94–F'02) received the B. E. degree in electronics engineering from Niigata University, Niigata, Japan, and the M. E. and Dr. Eng. degrees from the Tokyo Institute of Technology, Tokyo, Japan, in 1976, 1978, and 1983, respectively.

In 1978, he joined the Faculty of Engineering, Niigata University, where he is a Professor and Head of the Information Engineering Department. From 1988 to 1989, he was a Research Associate at the University of Illinois at Chicago. His interests are in the field of radar polarimetry, microwave sensing, and imaging.

Dr. Yamaguchi was Chair of the IEEE Geoscience and Remote Sensing Society Japan Chapter (2002–2003), Vice Chair (2000–2001), organizer of Polarimetric-Synthetic Aperture Radar Workshops (2000–2005) in Japan, and Associate Editor for Asian affairs of the GRSS Newsletter since 2003. He is a Fellow of the Institute of Electronics, Information and Communication Engineers, Japan, and was the recipient of the 2008 IEEE GRSS Education Award.



Gulab Singh (S'09–M'11) received his B.Sc. and M.Sc. degrees in physics from the Meerut University, Meerut, India in 1998 and 2000, respectively, and his M. Tech. degree in remote sensing from the Birla Institute of Technology, Ranchi, India in 2005 and his Ph.D. from Indian Institute of Technology Bombay,

Mumbai, India in 2010. He taught Physics to intermediate students for an academic session in 2002-2003 at Janta Inter College, Jhabiran, Saharanpur, India and from 2005 to 2007, he was Research Fellow at Indian Institute of Technology Bombay, Mumbai, India, where he was involved in several research projects related to POL-SAR and In-SAR data analysis for snow and ice parameters retrieval. He is currently Post Doctoral Fellow at Graduate School of Science and Technology, Niigata University, Niigata, Japan. His current research interests include SAR data analysis, SAR polarimetry and SAR interferometry techniques development for earth and lunar surface parameters estimation.



Sang-Eun Park (S'05–M'07) received the B.S. and M.S. degrees in geophysics and Ph.D. degree in radar remote sensing and geophysics from the Seoul National University, Seoul, Korea, in 2000, 2002, and 2007 respectively. From 2007 to September 2009, he worked at the Radar Polarimetry Remote Sensing Group of

the University of Rennes 1, Rennes, France, for a post-doctoral fellow on radar polarimetry. From October 2009 to January 2010, he was a project assistant in the Institute of Photogrammetry and Remote Sensing, Vienna University of Technology, Vienna, Austria. He is currently an Assistant

Professor in the Graduate School of Science and Technology at Niigata University, Japan. His research interests include polarimetric SAR classification, forward and Inverse modeling of microwave vegetation and surface backscattering, and investigation of multi-source data integration methodology.



Hirokazu Kobayashi (M'87–SM'10) was born in Hokkaido, Japan, on 1955.

He received the B.E.E. and M.E.E. degrees from the Shizuoka University, Shizuoka, Japan in 1978, 1980, respectively.

He joined Fujitsu LTD., Kawasaki, Japan at 1980. Since 1981 he has been with the Fujitsu System Integration Laboratories as a Researcher on developments for micro/millimeter wave wide-band antennas, active phased array systems and theoretical investigation for scattering cross sections. During 1999-2010, he served as General Manager of the laboratories and Fujitsu LTD. He received the Dr. Eng. degree from Tsukuba University, Tsukuba, Japan, in 2000. From 2010 he joined the Faculty of Engineering as a Professor in Niigata University, Niigata, Japan. His current research interests are high-frequency analysis for computing of radar cross-section of large objects and near-field analysis using PO/PTD/GTD, and near-field transformation to far-field based on microwave imaging theory (SAR/ISAR).

Dr. Kobayashi is a member of the Institute of Electronics, Information and Communication Engineers, Japan.